

A Tsunami Warning System based on Offshore Bottom Pressure Gauges and Data Assimilation for Crete Island in the Eastern Mediterranean Basin

Yuchen Wang¹, Mohammad Heidarzadeh², Kenji Satake¹, Iyan Eka Mulia¹, and Masaki Yamada³

¹University of Tokyo

²Brunel University London

³Shinshu University

November 24, 2022

Abstract

The Eastern Mediterranean Basin (EMB) is under the threat of tsunami events triggered by various causes including earthquakes and landslides. We propose a deployment of Offshore Bottom Pressure Gauges (OBPGs) around Crete Island, which would enable tsunami early warning by data assimilation for disaster mitigation. Our OBPG network consists of 12 gauges distributed around Crete Island. The locations of OBPGs are confirmed by Empirical Orthogonal Function (EOF) analysis of the pre-calculated tsunami scenarios, and most of them are placed at the locations where the most energetic wave dynamics occur. We demonstrate three test cases comprising a hypothetical seismogenic tsunami in east Sicily, a hypothetical landslide tsunami in the Aegean Sea, and the real tsunami event of the May 2020 off the Crete earthquake. Our designed OBPG network achieves a forecasting accuracy of 88.5 % for the hypothetical seismogenic tsunami and 85.3% for the hypothetical landslide tsunami with warning lead times of 10-20 min for both cases. For the real event of May 2020, it predicts the tsunami arrival at tide gauge NOA-04 accurately; the observed and forecasted amplitudes of the first wave are 5.0 cm and 4.5 cm, respectively. The warning lead time for the May 2020 event was \sim 10 min. Therefore, our results reveal that the assimilation of OBPG data can satisfactorily forecast the amplitudes and arrival times for tsunamis in the EMB. We note that further studies are necessary to examine the relation between the performance of the system and the number of OBPGs or the tsunami characteristics.

Supplementary Information for “A Tsunami Warning System based on Offshore Bottom Pressure Gauges and Data Assimilation for Crete Island in the Eastern Mediterranean Basin”

Yuchen Wang¹, Mohammad Heidarzadeh², Kenji Satake¹, Iyan E. Mulia¹, and Masaki Yamada³

¹Earthquake Research Institute, The University of Tokyo, Tokyo, Japan.

²Department of Civil & Environmental Engineering, Brunel University London, Uxbridge UB8 3PH, UK.

³Department of Geology, Faculty of Science, Shinshu University, Nagano, Japan.

Corresponding author: Yuchen Wang (ywang@eri.u-tokyo.ac.jp)

Comparisons of Tsunami Waveforms by Two-Layer/*JAGURS* Models

In this supplementary information, we compare the tsunami waveforms at Offshore Bottom Pressure Gauges (OBPGs) and tide gauges, which are simulated with different initial conditions in the propagation phase.

In our study, the generation phase ($t = 0 - 5$ min) of landslide tsunamis is simulated by the two-layer model. For the propagation phase, we adopt different models with different initial conditions: the two-layer model

(Kawamata et al., 2005; Ren et al., 2020) and *JAGURS* model (Satake, 1995; Baba et al., 2015). In the two-layer-model, the surface elevation and the horizontal velocities at the end of landslide generation phase ($t = 5$ min) are both used as the initial condition. We only consider the upper layer (sea-water layer) for the propagation phase modelling. However, in *JAGURS* model, we only use the surface elevation as the initial condition, because *JAGURS* model cannot load initial velocities (Baba et al., 2015). In both models, we compute the tsunami propagation in the region of $34.0\text{-}38.0N$, $20.0\text{-}30.0E$. The grid resolution is 30 arc sec, and the time step is 1 s. We simulate the tsunami propagation until 180 min after the landslide. The waveforms at OBPGs and tide gauges are recorded.

Figures S1 and S2 show the comparisons of tsunami waveforms at OBPGs and tide gauges, respectively. Blue curves indicate the tsunami whose propagation phase is simulated by the two-layer model, with the consideration of horizontal velocities at the end of landslide generation phase ($t = 5$ min). Red curves indicate the results of *JAGURS* model. In both figures, the waveforms simulated by two models are very similar. The tsunami simulated by the two-layer model arrives only slightly earlier than the one by *JAGURS* model. Hence, our results indicate that the horizontal velocities at the end of landslide generation phase is negligible for tsunami propagation modeling.

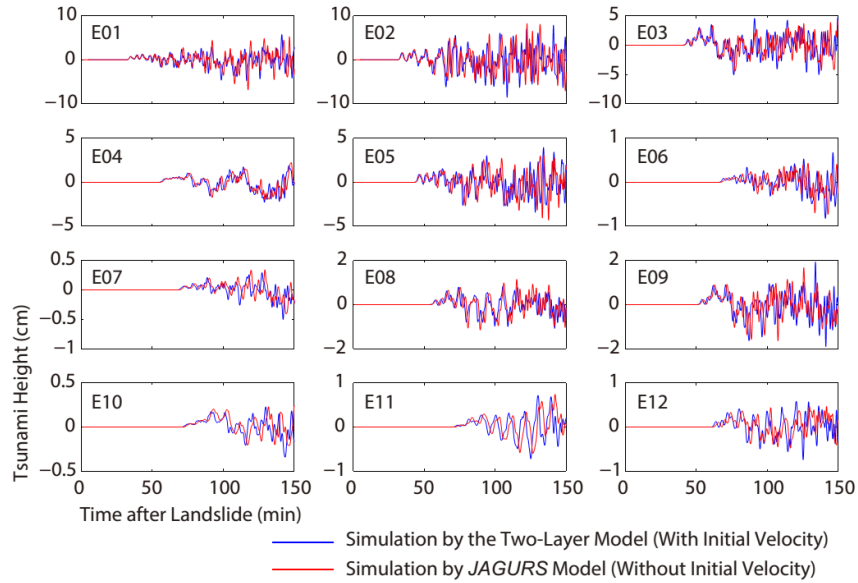


Figure S1 . Comparison of tsunami waveforms at OBPGs. The propagation phases are simulated by the two-layer model (blue curves) and *JAGURS* model (red curves), respectively.

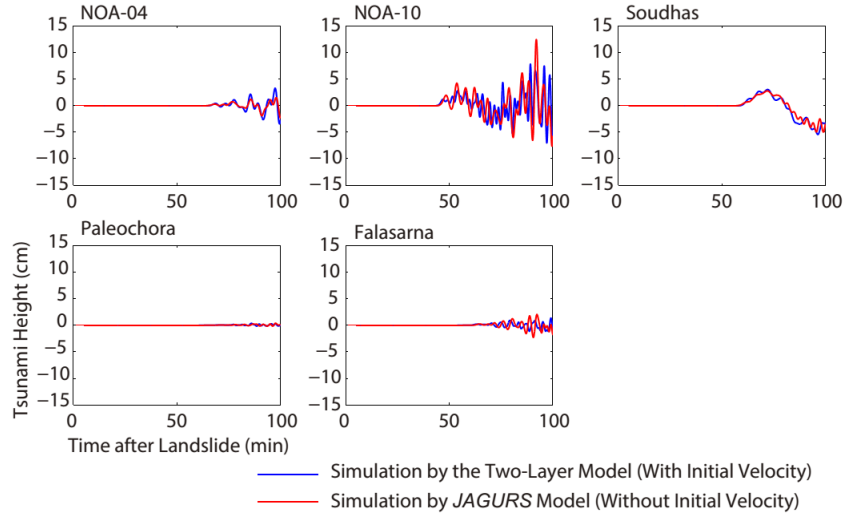


Figure S2 . Comparison of tsunami waveforms at tide gauges. The propagation phases are simulated by the two-layer model (blue curves) and *JAGURS* model (red curves), respectively.

References

- Baba, T., Takahashi, N., Kaneda, Y., Ando, K., et al. (2015). Parallel implementation of dispersive tsunami wave modeling with a nesting algorithm for the 2011 Tohoku Tsunami, *Pure Appl. Geophys.* , 172, 3433-3472, doi: 10.1007/s00024-015-1049-2.
- Kawamata, K., Takaoka, K., Ban, K., et al. (2005). Model of tsunami generation by collapse of volcanic eruption: The 1741 Oshima-Oshima tsunami, in *Tsunamis: Case Studies and Recent Developments* , edited by K. Satake, 79-96, Springer, New York.
- Ren, Z., Wang, Y., Wang, P., Hou, J., et al. (2020). Numerical Study of the Triggering Mechanism of the 2018 Anak Krakatau Tsunami: Eruption or Collapsed landslide? *Nat. Hazards* , 102, 1-13. doi:10.1007/s11069-020-03907-y.
- Satake, K. (1995). Linear and nonlinear computations of the 1992 Nicaragua earthquake tsunami. *Pure Appl. Geophys.* 144(3-4), 455-470. doi:10.1007/BF00874378.

1 **A Tsunami Warning System based on Offshore Bottom Pressure Gauges and Data**
2 **Assimilation for Crete Island in the Eastern Mediterranean Basin**

3
4 **Yuchen Wang¹, Mohammad Heidarzadeh², Kenji Satake¹, Iyan E. Mulia¹, and Masaki**
5 **Yamada³**

6
7 ¹Earthquake Research Institute, The University of Tokyo, Tokyo, Japan.

8 ²Department of Civil & Environmental Engineering, Brunel University London, Uxbridge UB8
9 3PH, UK.

10 ³Department of Geology, Faculty of Science, Shinshu University, Nagano, Japan.

11
12
13
14 Corresponding author: Yuchen Wang (ywang@eri.u-tokyo.ac.jp)

15
16
17 **Key Points:**

- 18 • A tsunami warning system is proposed for Crete Island, Greece, based on Offshore
19 Bottom Pressure Gauges and data assimilation.
- 20 • The designed system achieves a high accuracy in forecasting the arrival time and
21 amplitude for tsunamis in the Eastern Mediterranean Basin.
- 22 • Our method successfully forecasts the recent real tsunami of the 2 May 2020 off Crete
23 Island, Greece.

26 **Abstract**

27 The Eastern Mediterranean Basin (EMB) is under the threat of tsunami events triggered by
28 various causes including earthquakes and landslides. We propose a deployment of Offshore
29 Bottom Pressure Gauges (OBPGs) around Crete Island, which would enable tsunami early
30 warning by data assimilation for disaster mitigation. Our OBPG network consists of 12 gauges
31 distributed around Crete Island. The locations of OBPGs are confirmed by Empirical Orthogonal
32 Function (EOF) analysis of the pre-calculated tsunami scenarios, and most of them are placed at
33 the locations where the most energetic wave dynamics occur. We demonstrate three test cases
34 comprising a hypothetical seismogenic tsunami in east Sicily, a hypothetical landslide tsunami in
35 the Aegean Sea, and the real tsunami event of the May 2020 off the Crete earthquake. Our
36 designed OBPG network achieves a forecasting accuracy of 88.5 % for the hypothetical
37 seismogenic tsunami and 85.3% for the hypothetical landslide tsunami with warning lead times
38 of 10-20 min for both cases. For the real event of May 2020, it predicts the tsunami arrival at tide
39 gauge NOA-04 accurately; the observed and forecasted amplitudes of the first wave are 5.0 cm
40 and 4.5 cm, respectively. The warning lead time for the May 2020 event was ~10 min.
41 Therefore, our results reveal that the assimilation of OBPG data can satisfactorily forecast the
42 amplitudes and arrival times for tsunamis in the EMB. We note that further studies are necessary
43 to examine the relation between the performance of the system and the number of OBPGs or the
44 tsunami characteristics.

45

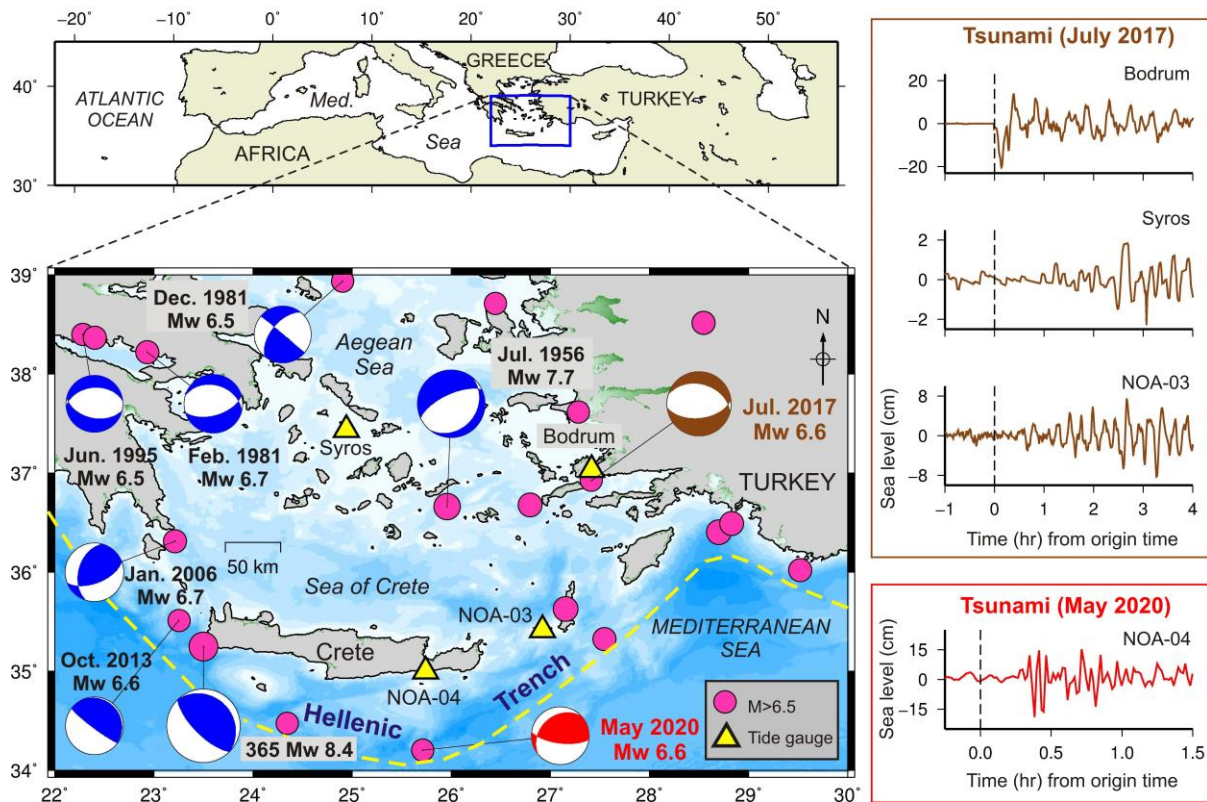
46 **1 Introduction**

47 Tsunamis in the Eastern Mediterranean Basin (EMB) have raised significant concern
48 over the past years, in particular following the July 2017 Bodrum-Kos (Turkey-Greece) and the
49 May 2020 off the Crete earthquakes and tsunamis (Figures 1-2) (Yalciner et al., 2017;

50 Heidarzadeh et al., 2017). In the catalogue of tsunamis in the Mediterranean Sea, Soloviev
51 (1990) identified numerous tsunami events in the Aegean Sea, Sea of Crete and other locations in
52 the EMB. The southern Greece, including Crete Island, the Cyclades and the Dodecanese
53 Islands, are among the most active regions in terms of seismicity. The main cause of tsunami
54 generation in this region is tectonic activity associated with strong earthquakes (Papadopoulos et
55 al., 2007a). For example, earthquakes often occur in the south-central Aegean Sea. The 1956
56 Amorgos earthquake (Mw 7.7-7.8) (Figure 1) was the largest one to strike Greece in the 20th
57 century. The 1956 earthquake generated a strong tsunami that affected the northern shores of
58 Crete Island. In Heraklion, the largest city in Crete, the 1956 tsunami arrived with a 2-m run-up
59 height and inundated 30 m inland. In Souda, a port city in the northwest of Crete Island, the
60 measured tsunami run-up height was 1.5 m (Okal et al., 2009). To the south of Crete Island, there
61 is an active tsunamigenic zone of the Hellenic subduction zone (Figure 1) which has produced
62 many large, shallow and intermediate-depth earthquakes in the past (Papadopoulos et al., 2007b).
63 For instance, the AD 365 earthquake (Mw 8.4) in the southwestern Crete Island was felt
64 throughout the eastern Mediterranean Sea. Its tsunami inundated coastal sites in Africa, the
65 Adriatic Sea, Greece, Sicily, and drowned thousands of people (Shaw et al., 2008). Moreover,
66 the tsunamigenic zone in the east Aegean Sea also has a very high tsunami potential.

67 The two recent events in the EMB region are the July 2017 Bodrum-Kos earthquake (Mw
68 6.6; Yalciner et al., 2017; Dogan et al., 2019) and the May 2020 off the Crete earthquake (Mw
69 6.6; USGS: the United States Geological Survey). The 2017 event occurred near the Turkey-
70 Greece border and generated a moderate tsunami that caused damage in Bodrum Peninsula and
71 in Kos (Heidarzadeh et al., 2017; Yalciner et al., 2017). The tsunami was recorded by several
72 tide gauges in the region (Figure 1) and caused some moderate damage with no casualties. The

73 tsunami was also recorded by a tide gauge in the Kasos Island, approximately 30 km to the east
 74 of Crete (i.e, station NOA-03) (Figure 1). The May 2020 tsunami occurred south of Crete Island,
 75 following an Mw 6.6 earthquake. There were no reports of injuries or casualties in the aftermath
 76 of this event. The earthquake generated a tsunami that hit the southern coast of Crete Island at
 77 around 15-20 min after the earthquake and was recorded at tide gauge NOA-04 with tsunami
 78 amplitudes of 15 – 20 cm (Figure 1).



79
 80 **Figure 1.** Location of Crete Island and the past earthquakes/tsunamis in the surrounding areas.
 81 The tsunami waveforms of the July 2017 Bodrum-Kos earthquake and the May 2020 off the
 82 Crete earthquake are plotted in the right panels. The focal mechanisms and magnitudes are based
 83 on USGS (the United States Geological Survey) earthquake catalogue.

85 In addition to earthquakes, tsunamis in the EMB are also generated by landslides and
86 volcanic eruptions (Yalciner et al., 2014; Samaras et al., 2015). Papadopoulos et al. (2007a)
87 studied 32 reliable cases of landslide tsunamis in the Mediterranean Sea. On 30 September 1650,
88 a large tsunami occurred during the eruption of the submarine volcanic edifice Kolumbo in the
89 Aegean Sea. It was generated by the submarine collapse of the volcanic cone (Dominey-Howes
90 et al., 2000). The tsunami violently swept ships and fishing boats at Crete Island, and the wave
91 overtopped the city's sea walls (Papadopoulos et al, 2007a). Yalciner et al. (2014) studied
92 generation and propagation of landslide tsunamis in the EMB.

93 For disaster mitigation proposes, it is important to design an observational system aimed
94 at tsunami early warning. Tsunami data assimilation, a recent technology for tsunami warning,
95 relies on Offshore Bottom Pressure Gauges (OBPGs) which monitor the sea surface elevation
96 and report the data in real time (Satake, 2014; Maeda et al., 2015; Heidarzadeh and Gusman,
97 2018). In the Nankai Trough offshore west Japan, a dense array of OBPGs known as DONET
98 (the Dense Oceanfloor Network system for Earthquakes and Tsunamis) (Kaneda, 2010) have
99 been deployed and is available for tsunami warning system. However, in the EMB such
100 observational system is presently unavailable. In this study, we propose a potential tsunami early
101 warning system for Crete Island based on the deployment of OBPGs. The system forecasts the
102 tsunami by data assimilation approach. We demonstrate that our designed OBPG network is
103 useful for forecasting both seismogenic and landslide tsunamis, by conducting experiments with
104 two hypothetical tsunamis and the real tsunami of 2 May 2020.

105

106 **2 Data and Method**

107

108 **2.1 Empirical Orthogonal Function (EOF) Analysis for Optimal Location of the OBPGs**

109

110 Empirical Orthogonal Function (EOF) analysis, also known as the Principal Component
 111 Analysis (PCA), is commonly used to decompose the data into spatial and temporal modes
 112 (Lorenz, 1956; Liu et al., 2018). The EOF spatial modes provide information about the areas
 113 where the modal activity is the highest, which correspond to the main energy distribution of a
 114 system (Cohen et al., 2003). OBPGs are used to detect the tsunami signals, and hence for an
 115 optimal network, they should be placed at the locations where the energetic dynamics occur. In
 116 our study, we apply EOF analysis to confirm our proposed locations of observational points (i.e.
 117 locations of OBPGs).

118 Assuming that there are n locations (grid points), and each location has a time series of
 119 length p , we create an $n \times p$ matrix \mathbf{Z} that stores these data. The i^{th} column of such a matrix
 120 contains the time series at the i^{th} location (grid), while the j^{th} row represents a snapshot of the
 121 whole region at the j^{th} time step (Navarrete et al., 2020). After removing the mean of each time
 122 series, the covariance matrix is formed by $\mathbf{R} = \mathbf{Z}^T \mathbf{Z}$. Then we solve the eigenvalue problem as
 123 formulated below:

$$124 \quad \mathbf{RC} = \mathbf{CA} \quad (1)$$

125 where \mathbf{C} is the matrix of eigenvectors \mathbf{c}_i , and \mathbf{A} is a diagonal matrix containing the eigenvalues
 126 λ_i . Each eigenvector presents a spatial mode, and the first EOF spatial mode is associated with
 127 the largest eigenvalue.

128 In our study, we select the region around Crete Island, within the geographical domain of
 129 $33\text{--}36^{\circ}\text{N}$, $22\text{--}28^{\circ}\text{E}$. We select the grids with a water depth of more than 300 m that cover the
 130 region of designed OBPGs. To perform the EOF analysis, we consider three tsunami scenarios
 131 which are called Mode Generating Scenarios (MGSs). The sources of the MGSs are adopted
 132 from the past real tsunami events in the EMB region, from west to east: the 2013 Platanos
 133 earthquake, the 1956 Amorgos earthquake, and the 2017 Bodrum-Kos earthquake (Figures 1-2).
 134 We adopt the same parameters of fault locations and focal mechanisms (Table 1), but amplify the
 135 slip values of each scenario (Table 1; last column) when computing the MGSs, in order to make
 136 the tsunami amplitude more evident in the EOF analysis area. The simulation of tsunami
 137 propagation and generation of three MGSs is described in section 2.2. After performing the EOF
 138 analysis, we check whether our designed OBPGs are placed at locations with large absolute EOF
 139 values.

140 **Table 1.** Parameters of three Mode Generating Scenarios (MGSs) used in this study for our EOF
 141 analysis.

Scenario Number	Lon ($^{\circ}\text{E}$)	Lat ($^{\circ}\text{N}$)	Depth (km)	Strike ($^{\circ}$)	Dip ($^{\circ}$)	Rake ($^{\circ}$)	Length (km)	Width (km)	Slip (m)
1 (2013-like event)	35.50	23.28	60.0	127	83	88	90.0	40.0	7.0
2 (1956-like event)	36.72	25.76	25.0	39	25	246	81.0	41.0	7.0
3 (2017-like event)	36.93	27.41	7.0	285	39	-73	25.0	15.0	8.0

142

143

144 2.2 Simulation of Seismogenic Tsunamis

145

146

147

148

149

150

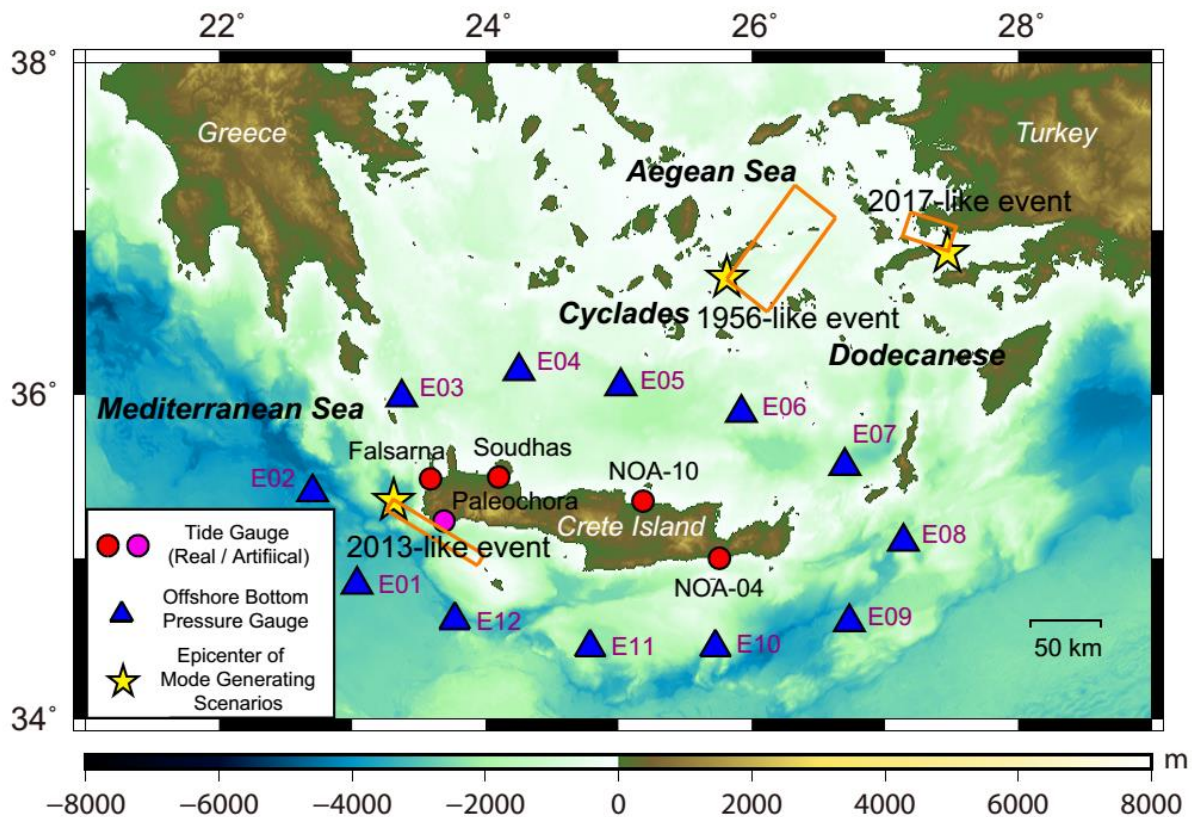
151

152

153

154

We adopt the analytical dislocation model of Okada (1985) to compute the seafloor deformation for seismogenic tsunamis. The sea surface displacement is assumed to be the same as the seafloor deformation and is used as the initial condition for tsunami simulation according to the common practice in tsunami science (e.g. Satake, 2015). Then, we apply a linear long-wave model to simulate tsunami propagation, using the simulation package *JAGURS* (Satake, 1995; Baba et al., 2015). Tsunami computation is performed on the supercomputer of Earthquake Information Center, The University of Tokyo. For computing the tsunamis arising from our three MGSs, the simulation time is 60 min since the earthquake origin time, and the spatial variation of water surface is stored every 10 s, resulting in 360 snapshots.



155

156 **Figure 2.** Locations of 12 designed Offshore Bottom Pressure Gauges (OBPGs) for the area
157 around Crete Island in the Eastern Mediterranean Basin (blue triangles). Red circles are the real
158 tide gauges on the island for waveform comparison. The pink circle is an artificial tide gauge
159 considered in this study. Yellow stars indicate the epicenter of Mode Generating Scenarios
160 (MGSs), and the orange rectangles indicate the locations and orientations of the faults.

161

162 The bathymetry and topography dataset are derived from the General Bathymetric Chart
163 of the Ocean released in 2014 (GEBCO_2014; Weatherall et al., 2015). We use a grid size of 30
164 arc sec (equivalent to ~925 m), and a time step of 1 s to satisfy the stability condition of Finite
165 Difference Method. The simulated tsunami waveforms at the locations of the proposed OBPGs
166 are used for data assimilation retrospectively. The waveforms recorded at tide gauges are
167 employed for waveform comparison in order to examine the performance of our method. Four
168 real and one artificial tide gauges around Crete Island are selected (Figure 2) which are: NOA-
169 04, NOA-10, Soudhas, Paleochora, and Falasarna. The stations of NOA-04 and NOA-10 are
170 operated by the National Observatory of Athens (NOA). The station Soudhas belongs to the
171 Permanent Service for Mean Sea Level (PSMSL). The station Paleochora serves as an
172 Inexpensive Device for Sea Level Measurement (IDSL), which is developed by the Joint
173 Research Centre (JRC) of the European Commission. The station Falasarna is a virtual tide
174 gauge, intended to evaluate the tsunami hazards of the west Crete Island in our study.

175

176 **2.3 Simulation of Landslide Tsunamis**

177

178 To assess the tsunami hazards in the EMB thoroughly, we also consider tsunamis
179 triggered by landslides. We use a two-layer hydrodynamic model to simulate the generation and
180 propagation of landslide tsunamis (Maeno and Imamura, 2011; Ren et al., 2020).

181 Here we assume that a submarine landslide occurs in the Cyclades region. We focus on a
182 smaller region of $36.5\text{--}37.5^\circ\text{N}$, $25.0\text{--}26.0^\circ\text{E}$, and resample the GEBCO_2014 grid to a finer
183 resolution of 6 arc sec. The time step is 0.1 s for modeling the generation phase of landslide
184 tsunami. In our two-layer model, the slides are simulated as the bottom layer whose motion is
185 fully coupled to that of the surrounding water. The submarine landslide layer is of arbitrary
186 geometry and is represented as a dense Newtonian fluid. Additional information about landslide
187 modeling process and associated hydrodynamic equations are given in Kawamata et al. (2005)
188 and Ren et al. (2020). We simulate the landslide and the triggered tsunami for the first five
189 minutes (i.e., the generation phase). Then, we compute the tsunami propagation in a larger region
190 of $34.0\text{--}38.0^\circ\text{N}$, $20.0\text{--}30.0^\circ\text{E}$, with a resolution grid of 30 arc sec, and a time step of 1 s, using
191 the two-layer/*JAGURS* models. In the two layer-model, the surface elevation and the horizontal
192 velocities at the end of landslide generation phase are used as the initial condition, while only the
193 surface elevation was used in *JAGURS* model for tsunami propagation (Satake, 2012;
194 Heidarzadeh et al., 2014). Comparison of these two models are shown in Supplementary
195 Information, which shows that they are similar. This might indicate the horizontal velocity at the
196 end of landslide generation phase is negligible for tsunami propagation modeling. In our
197 experiment of the hypothetical landslide tsunamis, we adopted the results of the two-layer model.

198 **2.4 Tsunami Data Assimilation**

199

200 Tsunami data assimilation is a tsunami early warning approach which does not require
 201 information about fault parameters but directly applies sea surface elevation data for tsunami
 202 forecast (Maeda et al., 2015; Gusman et al., 2016). It successively assimilates the real-time
 203 offshore sea surface observation, and estimates the regional tsunami status. Wang et al. (2019)
 204 applied this approach to the 2015 Torishima volcanic tsunami earthquake retrospectively, and
 205 successfully forecasted the tsunami height and arrival time only based on offshore sea surface
 206 observations. Recently, this approach is also taken into consideration when designing the
 207 offshore observational devices. For example, Heidarzadeh et al. (2019) proposed a potential
 208 deployment of OBPGs in the western Mediterranean Sea. Navarrete et al. (2020) designed a
 209 network of tsunameters off the Chilean coast based on tsunami data assimilation.

210 The tsunami status at n -th time step is represented as:

211 $\mathbf{x}_n = (h(n\Delta t, x, y), M(n\Delta t, x, y), N(n\Delta t, x, y))$, where h is the sea surface height, M and N are
 212 horizontal flow fluxes in the x and y directions, respectively, and Δt is the time step for
 213 numerical simulations. M and N are defined as: $M = u(d + h)$ and $M = v(d + h)$ where u and
 214 v are horizontal velocities in the x and y directions, respectively, and d is water depth. The
 215 tsunami status is forecasted by multiplying the tsunami status of last time step with a propagation
 216 matrix \mathbf{F} , which is built from the tsunami propagation model (Equation 2). Here the superscripts
 217 f and a refer to forecasted (before correction) and assimilated (after correction) tsunami status,
 218 respectively.

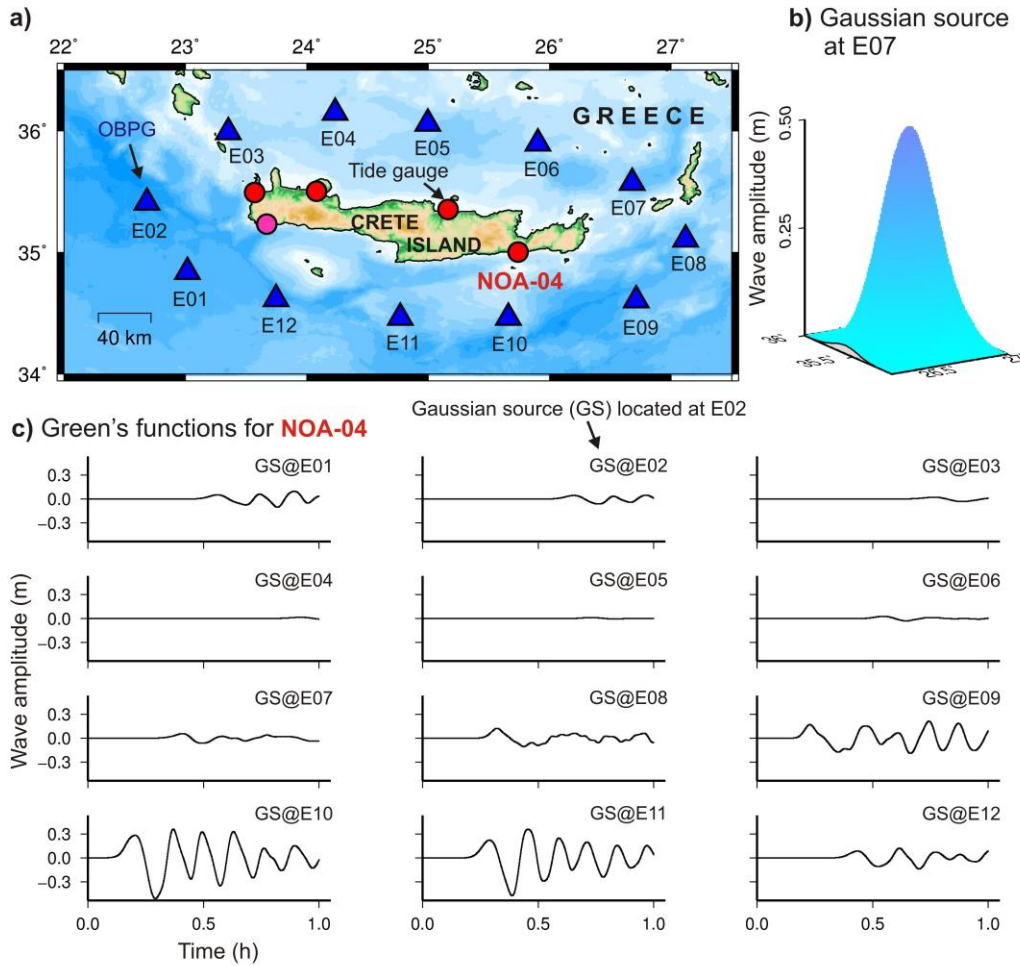
219

$$\mathbf{x}_n^f = \mathbf{F}\mathbf{x}_{n-1}^a \quad (2)$$

220

$$\mathbf{x}_n^a = \mathbf{x}_n^f + \mathbf{W}(\mathbf{y}_n - \mathbf{H}\mathbf{x}_n^f) \quad (3)$$

221 where matrix \mathbf{H} is a sparse matrix that extracts the forecasted tsunami height of the
222 corresponding stations, matrix \mathbf{W} is a weight matrix for smoothing which is used to bring the
223 forecasted tsunami status closer to the real wavefield, and \mathbf{y}_n is real tsunami observation data
224 that is obtained from the OBPGs. More details about the weight matrix \mathbf{W} are described in
225 Maeda et al. (2015). In Equation 3, the forecasted tsunami status (i.e., \mathbf{x}_n^f) is corrected by
226 observation. The offshore OBPGs provide the data of tsunami height (h); then, tsunami flow
227 velocities (u and v) are reconstructed during the assimilation process. After correction, we obtain
228 the assimilated tsunami status \mathbf{x}_n^a , and it will be used for further forecasting in the next time step.
229 During the assimilation process, Equations 2 and 3 are iterated repeatedly at each time step.
230 Therefore, we are able to forecast the tsunami status based on the observation of OBPGs. In
231 order to improve the efficiency of data assimilation, we adopt the technique of Green's Function-
232 based Tsunami Data Assimilation (GFTDA; Wang et al., 2017; Furumura et al., 2018). We
233 calculate the Green's functions between the proposed OBPGs and the tide gauges (Figure 3a-c),
234 and we use them to synthesize the forecasted tsunami waveforms during the assimilation process.



235

236 **Figure 3.** Green's Function-based Tsunami Data Assimilation (GFTDA). (a) The Green's
 237 function is defined as the waveform of tsunami propagation from an OBPG to a tide gauge
 238 (Wang et al., 2017). (b) The initial Gaussian-shaped source located at the OBPG station of E07
 239 for calculating Green's functions. (c) The Green's functions for tide gauge NOA-04. There are
 240 12 Green's functions that are resulted from each OBPG.

241

242 **3 Application and Results**

243

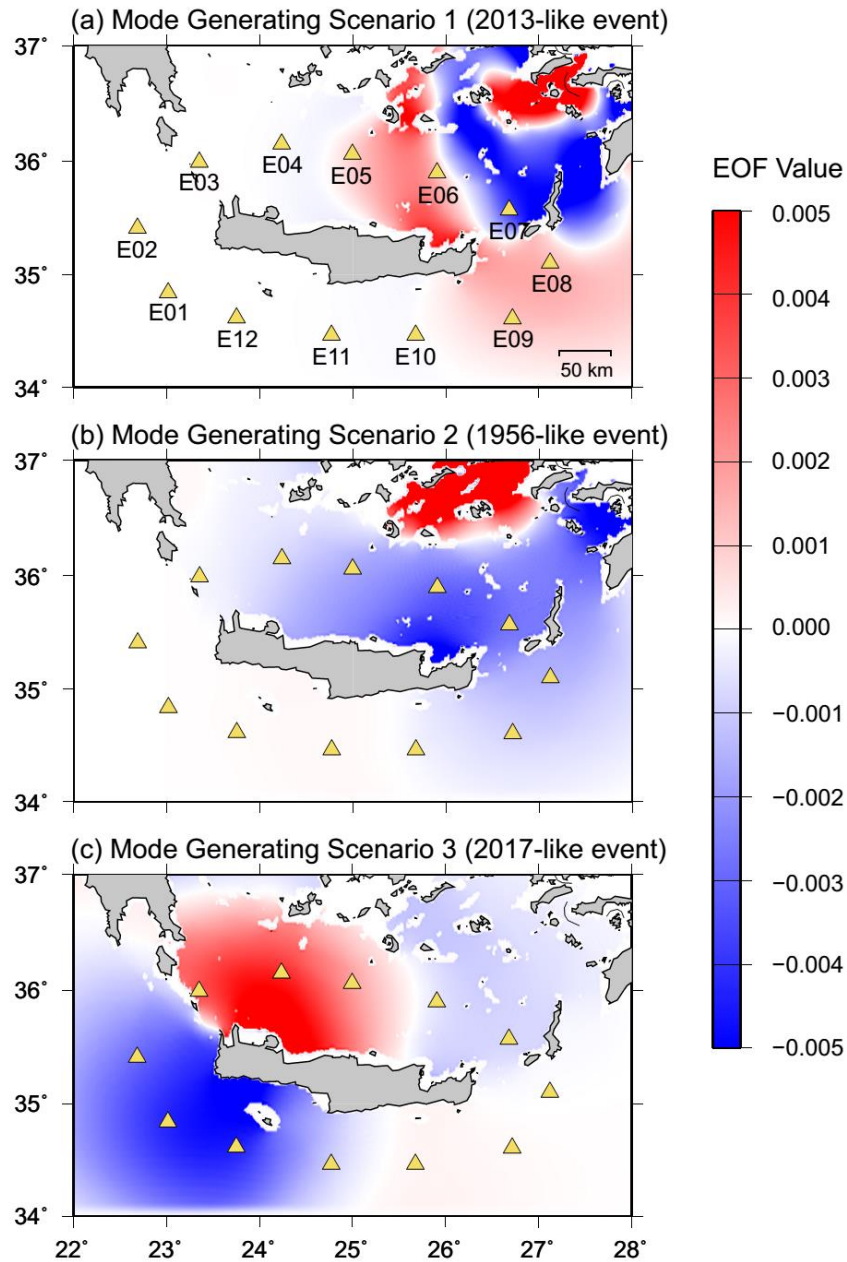
244 **3.1 OBPG Locations and EOF Results**

245

246 A total number of 12 OBPGs are selected for the observational network. They are located
247 around Crete Island and cover all directions (Figures 3-4). The design of OBPG locations is
248 under the constraint that they are at least 30 km apart from each other, in order to keep a large
249 spatial coverage (Navarrete et al., 2020). We also consider that the OBPGs are distanced at least
250 50 km from the coast, in order to provide early warnings before tsunami arrival.

251 The first EOF spatial modes for three MGSs are plotted in Figure 4. For each EOF mode,
252 there is a value of variance which represents its contribution to the total energy (Lorenz, 1956).
253 For the three MGSs, i.e., the 2013-like event, the 1956-like event, and the 2017-like event, the
254 variances of the first EOF mode are 36.8%, 51.1% and 41.2%, respectively. Since the variance of
255 the first EOF mode is considerably larger than that of subsequent EOF modes (e.g., the second
256 and third modes), using only the first EOF mode is sufficient to quantify the total energy of the
257 tsunami dynamics in deep water (Mulia et al., 2019). It can be seen that most OBPGs are located
258 at the areas with a large absolute EOF value for at least one MGS (Figure 4a-c). For stations E06
259 and E07, they appear in the areas with large absolute values in both MGS1 and MGS2. The
260 station E05 is located in the energetic regions of both MGS1 and MGS3. Hence, we confirm that
261 most of our proposed OBPGs are placed at the locations where energetic dynamics occur.

262 We note that the OBPG network is designed for providing warning to Crete Island as a
263 pilot location. Therefore, in case the target of the warning system is another coastal location or a
264 combination of locations, the same approach can be applied to design an optimal OBPG network
265 for those cases.



266

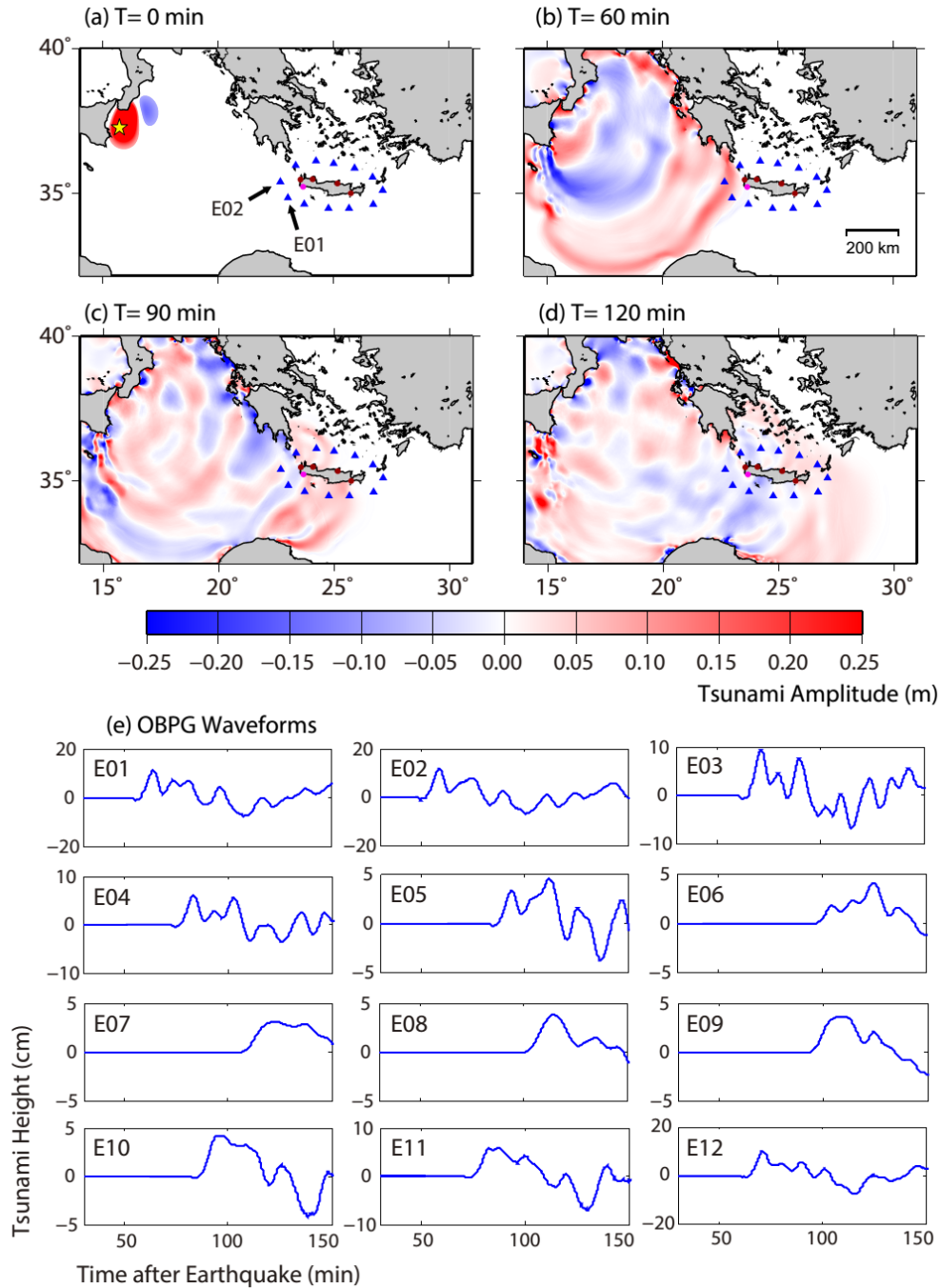
267 **Figure 4.** The first EOF spatial mode of three MGSs which are used for confirming the selection
 268 of the OBPG locations. Most of OBPGs are located in the points with large EOF values (absolute
 269 values) of at least one MGS.

270

271 **3.2 Early Warning for Hypothetical Seismogenic Tsunamis**

272

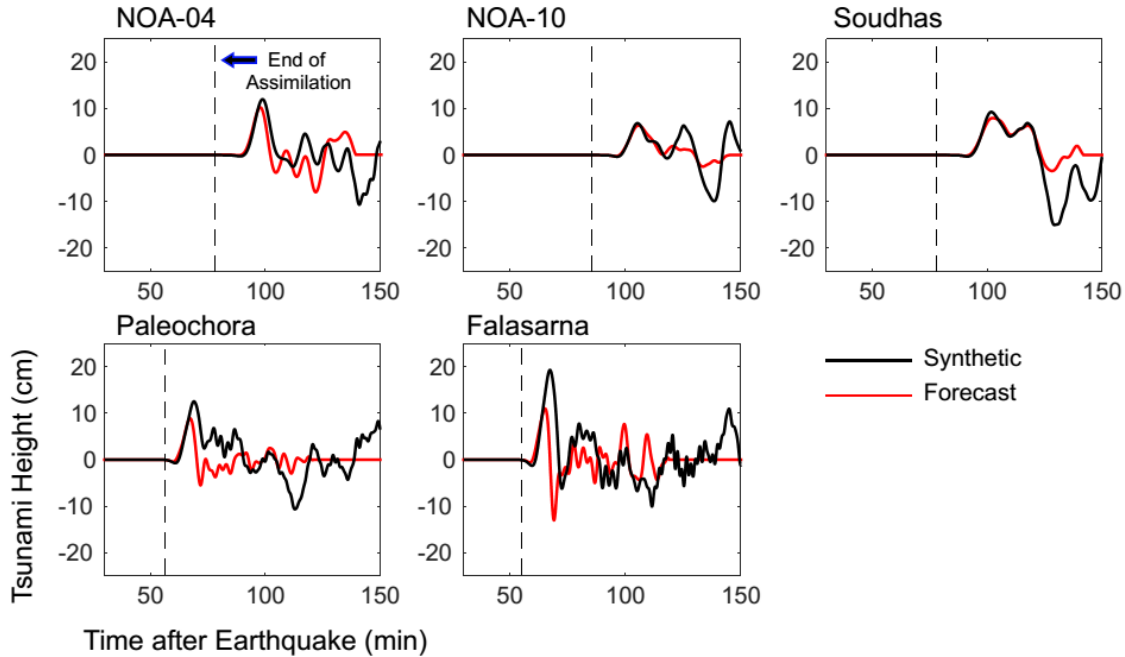
273 Our first test is for a relatively far-field tsunami originating from the east Sicily, at the
274 distance of approximately 900 km from Crete Island. The hypothetical earthquake (Mw 7.9) in
275 east Sicily has a fault with a dimension of 95.0 km \times 45.0 km, and its epicenter is located at
276 37.266°N, 15.686°E. The depth is 35.0 km. The strike, dip and rake angles of the hypothetical
277 earthquake are 20°, 42° and 121°, respectively, with a slip of 7.0 m. Figure 5a shows the initial
278 sea surface deformation produced by this earthquake. It generates a tsunami that propagates
279 towards the EMB (Figure 5b-d). The rationale for this scenario is based on the study by Soloviev
280 (1990) who informed that east Sicily is a major tsunamigenic zone in the EMB. Crete Island is
281 along the direction of the short axis of the seismic fault (i.e. fault width), and thus the tsunami
282 energy is more concentrated towards this island. The tsunami waveforms obtained through
283 forward tsunami simulation are called “synthetic waveforms” here which are shown in Figure 5e.
284 The first tsunami peak arrives at the stations E02 and E01 at 59 min and 64 min after the
285 earthquake, respectively (Figure 5e). The arrival times are 67 min and 69 min at the tide gauges
286 Falasarna and Paleochora, respectively. The maximum tsunami amplitude of 19.3 cm is recorded
287 at the tide gauge Falasarna. It has a comparatively smaller effect (< 10.0 cm) on the tide gauge
288 NOA-10, because it is located on the eastern side of the island (Figure 6).



289

290 **Figure 5.** (a): Initial sea surface deformation due to the hypothetical earthquake in east Sicily.
 291 (b)-(d): Tsunami snapshots of the hypothetical seismogenic tsunami generated by an earthquake
 292 in east Sicily. (e): The synthetic waveforms at OBPGs from tsunami simulation that are used as
 293 input waveforms for data assimilation. The yellow star represents the epicenter of the
 294 earthquake.

295



296

297 **Figure 6.** Comparison of the synthetic (black curves) and forecasted waveforms using data
 298 assimilation (red curves) at five tide gauges on Crete Island. The dashed vertical line indicates
 299 the end of the time window for tsunami data assimilation.

300

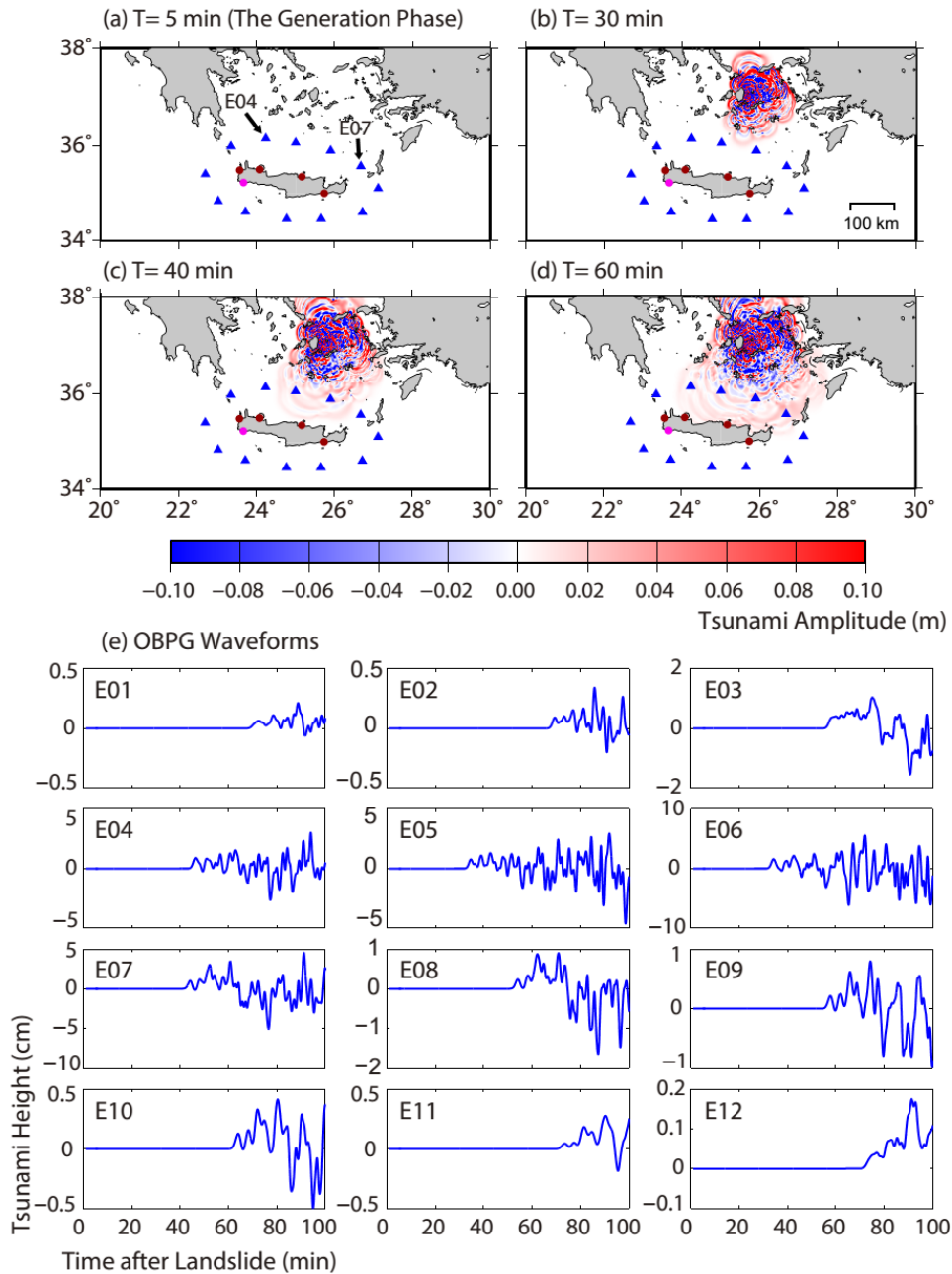
301 The tsunami waveforms are forecasted using data assimilation approach and are updated
 302 continuously during the data assimilation process. The tsunami waveforms obtained by data
 303 assimilation are called “forecasted waveforms” here (Figure 6; red waveforms), which are
 304 compared with synthetic waveforms (Figure 6; black waveforms). The dashed line in Figure 6
 305 indicates the end of data assimilation process. Therefore, the time interval between the end of the
 306 assimilation (i.e. dashed line in Figure 6) and the arrival of the tsunami at each tide gauge is the
 307 lead time for issuing tsunami warnings. At tide gauges NOA-4, NOA-10 and Soudhas, the lead
 308 time for tsunami warning is approximately 20 min. At Paleochora and Falasarna, the warning
 309 lead time is relatively shorter (i.e. approximately 10 min) due to the relatively short distance
 310 between the tide gauge and the OBPGs. Figure 6 indicates that our data assimilation approach

311 forecasts the tsunami arrival times and amplitudes at all tide gauges well. At NOA-04, NOA-10
312 and Soudhas, the amplitude of the first tsunami peak is accurately predicted by data assimilation.
313 But at Falasarna, the forecasted amplitude (i.e. 11.0 cm) is smaller than the synthetic amplitude
314 that is used for comparison (19.3 cm). According to the performance quality index of Tsushima
315 et al. (2011), the tsunami forecast accuracy (i.e. percentage of success) is calculated by: $\left[1 - \right.$
316 $\left. \frac{\sum_{i=1}^N (O_i - F_i)^2}{\sum_{i=1}^N (O_i)^2} \right] \times 100\%$. Here, O_i and F_i are the first-peak amplitude of the synthetic (used as
317 observation) and forecasted tsunamis, respectively. Overall, the accuracy of data assimilation
318 process for tsunami forecasting is 88.5% for a tsunami source in east Sicily.

319 **3.3 Early Warning for Hypothetical Landslide Tsunamis**

320

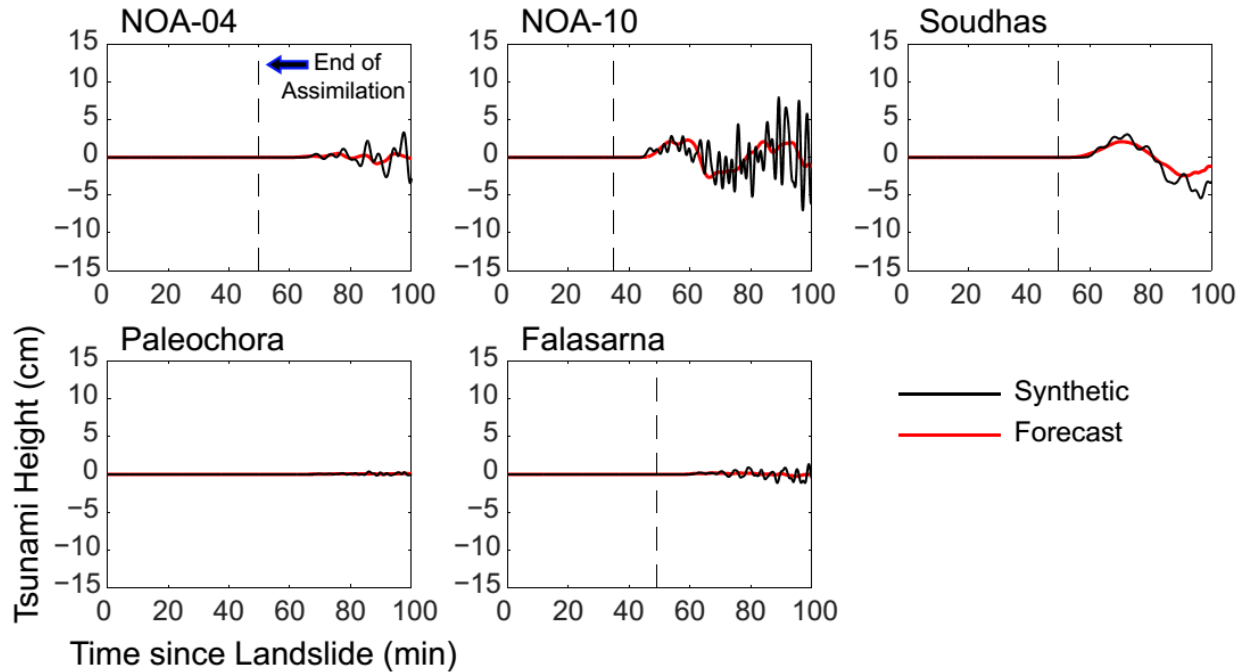
321 The tsunami generated by a landslide in Cyclades mainly affects the northern side of
322 Crete Island (Figure 7a-d). We assume that a submarine landslide occurs at 37.0°N and 25.7°E.
323 The region of the landslide is assumed to be a circle with a diameter of 1.5 km. The total amount
324 of landslide volume is assumed to be 0.3 km³, and the average thickness of the sliding mass is
325 170 m. The rationale for this scenario is based on the studies by Soloviev (1990) and Samaras et
326 al. (2015) who showed that seismic activities in the Aegean Sea region have triggered
327 tsunamigenic submarine landslides such as the events of the 1650 (M 6.3) and the 1968 (M 6.8).



328

329 **Figure 7.** (a): Initial condition for modeling the tsunami generated by the landslide (i.e., the
 330 generation phase). (b)-(d): Tsunami snapshots of the hypothetical landslide tsunami generated in
 331 Cyclades in the Aegean Sea. (e): The synthetic waveforms at OBPGs from forward tsunami
 332 simulation that are used as input waveforms for data assimilation.

333



334

335 **Figure 8.** Comparison of the synthetic (black curves) and forecasted waveforms (red curves) at
 336 five tide gauges on Crete Island. The dashed vertical line indicates the end of the time window
 337 for tsunami data assimilation.

338

339 The designed OBPBs on the north of Crete Island (E04 – E07) received evident tsunami
 340 signals from this hypothetical landslide tsunami, but the tsunami heights of other OBPBs are less
 341 than 2.0 cm (Figure 7). Compared to the seismogenic tsunami, the landslide tsunami has a
 342 shorter wavelength, and there are more high-frequency components and dispersive
 343 characteristics in their waveforms. Hence, it is challenging to distinguish the arrival time of the
 344 first tsunami peak. Assuming the time of the landslide initiation as $t = 0$, the first tsunami peak
 345 arrives at $t = 54 \text{ min}$ at tide gauge NOA-10 with an amplitude of 2.8 cm (Figure 8). The
 346 maximum peak, which is 7.8 cm in amplitude, arrives later at NOA-10. At tide gauge Soudhas,
 347 the first peak arrives at $t = 68 \text{ min}$ with an amplitude of 2.7 cm. The tsunami heights are

348 smaller (< 3 cm) at tide gauges NOA-04 and Falasarna. Almost no tsunami signal can be seen at
349 Paleochoira.

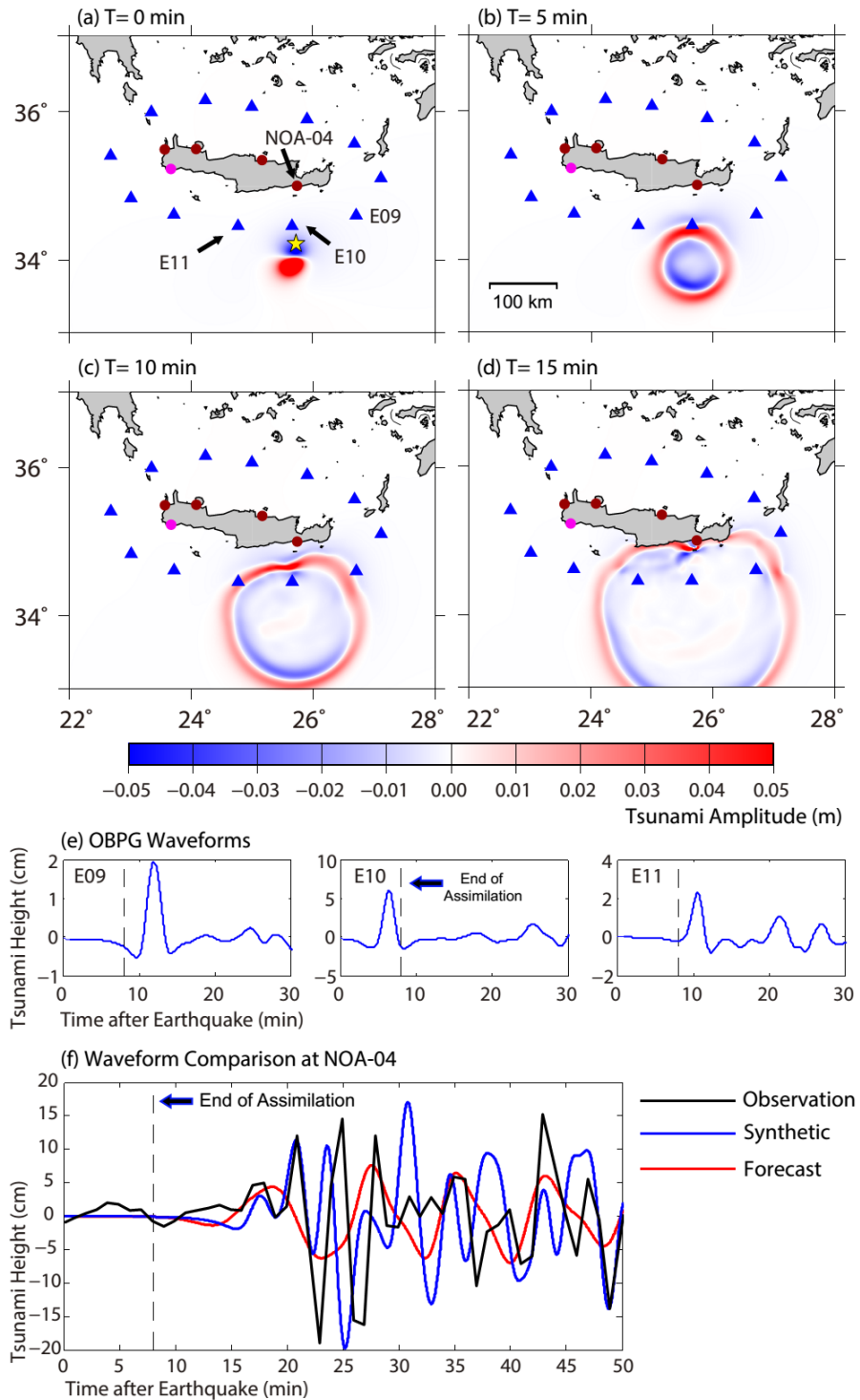
350 The waveforms are forecasted at 10 min before the arrival of the tsunami's first peak by
351 data assimilation approach (Figure 8). At both NOA-10 and Soudhas, the tsunami waveforms
352 that are forecasted by data assimilation are consistent with the simulations (Figure 8), though the
353 forecasted waveforms have less high-frequency components. At NOA-10, the tsunami arrival
354 time and the first-peak amplitude are predicted accurately, but the maximum amplitude is not
355 forecasted well. At Soudhas, the first-peak amplitude and the maximum amplitude are precisely
356 forecasted. At NOA-04, our forecasted waveforms generally match with the simulation, but At
357 Falasarna, it fails to predict the tsunami waveforms with a very small amplitude (i.e. < 3 cm).
358 Overall, considering the waveforms at tide gauges except for Paleochoira, the forecast accuracy
359 of our data assimilation approach for a hypothetical landslide tsunami is 85.3%.

360 **3.4 Early Warning for the May 2020 off the Crete Tsunami**

361
362 Besides hypothetical experiments, we also retrospectively use the tsunami generated by
363 the 2 May 2020 earthquake (Mw 6.6) offshore Crete Island as a test case. The tsunami was
364 recorded by the tide gauge NOA-04 on Crete Island (Figure 1). As there are no OBPGs located
365 off the coast, we use the synthetic waveforms as the input for data assimilation. To compute the
366 synthetic waveforms at OBPGs, we invert the tsunami data recorded at NOA-04 and estimate the
367 source model of the 2020 event. A single fault with a dimension of $20.0 \text{ km} \times 12.0 \text{ km}$ and a
368 slip of 1.5 m is used as the source of the tsunami. The epicenter is at 34.205°N , 25.712°E , and the
369 top depth of the fault is 11.5 km based on the USGS. The strike, dip and rake angles are 229° ,

370 31° and 46°, respectively, following the W-phase focal mechanism solution of the USGS for this
 371 event. Figure 9a shows the initial sea surface deformation caused by this earthquake.

372



373

374 **Figure 9.** (a): Initial sea surface deformation due to the May 2020 off the Crete earthquake. (b)-
375 (d): Tsunami snapshots generated by the May 2020 event. (e): The synthetic waveforms at
376 OBPGs from forward tsunami simulation that are used as input waveforms for data assimilation.
377 (f): Comparison of the observed (black curve), synthetic (blue curve) and forecasted waveforms
378 (red curve) at tide gauges NOA-04. The dashed vertical line indicates the end of the time
379 window for tsunami data assimilation. The yellow star represents the epicenter of the earthquake.
380

381 Figure 9b-d demonstrates the propagation of the tsunami and its wavefield. The tsunami
382 arrives at E10 at around 5 min after the earthquake whereas it arrives at the southern coast of
383 Crete Island at around 15 min after the earthquake. The tsunami waveforms at OBPGs obtained
384 through numerical simulation are used for data assimilation (Figure 9e). In Figure 9e, we only
385 plot the waveforms of the OBPGs where the tsunami arrives earlier than at tide gauge NOA-04.
386 This means we apply only three OBPG records of E09, E10 and E11 for forecasting the tsunami
387 at the coastal location NOA-04. The data assimilation process ends at 8 min after the earthquake,
388 which is indicated by the dashed line in Figure 9e-f.

389 The forecasted waveform using data assimilation is compared with the real observation
390 and the synthetic waveform (Figure 9f). The synthetic waveform is consistent with the real
391 observations for the first few waves, proving the validity of our source model and that the
392 waveforms at OBPGs are reliable for tsunami data assimilation. Our method predicts the tsunami
393 arrival at tide gauge NOA-04 accurately and it fairly forecasts the tsunami amplitude as well. For
394 the first tsunami peak, the observed and forecasted amplitudes are 5.0 cm and 4.5 cm, which are
395 very close with an accuracy of 99.0% calculated by the equation of quality index (Tsushima et
396 al., 2011), and the observed and forecasted arrival times are 18 min and 19 min, respectively. For
397 the later phase, the assimilated waveform has a longer wavelength, but it fairly predicts the

398 tsunami peaks at ~28 min and 35 min. Because the assimilation process ends after 8 min, the
399 tsunami warning lead time is ~10 min for the May 2020 event. Overall, the performance of the
400 OBPG network in predicting the real May 2020 tsunami appears to be satisfactory despite its
401 rather short arrival time of ~20 min. We note that the longer period of the forecasted wave (red
402 waveform) is due to the small size of the tsunami source which is shorter than the distance
403 between the two adjacent OBPGs (Figure 9a). In many cases of data assimilation efforts in the
404 past, the size of a tsunami source spans at least several OBPGs. Therefore, it is believed that the
405 result shown in Figure 9 for the May 2020 event is very important because it proves the success
406 of the method even for small tsunamis.

407

408 **4 Discussion**

409 Unlike trans-Pacific tsunamis, tsunamis in the EMB propagate in a narrow and confined
410 region (e.g. Heidarzadeh and Satake, 2013) and thus tsunamis could propagate across the
411 Mediterranean Sea in a short time (< 1 h) and arrive at the coastal areas. The OBPGs designed in
412 our study for the EMB are located in the narrow water body of the Mediterranean Sea and are
413 aimed at detecting tsunamis and assimilating the observed data into early warning in a short
414 time; mostly less than 30 min. For the data assimilation approach, we need sufficient
415 observational data in order to provide accurate forecasts. In our test of the real tsunami of 2 May
416 2020, the earthquake occurred in the near-field at the distance of ~100 km from the coast, and the
417 proposed OBPG station E10 is very close to the source region. In some cases, if the OBPG is
418 located within the source regions, non-hydrostatic response may cause ocean bottom pressure
419 perturbations not proportional to sea surface height. To overcome this problem, we could use the
420 method developed by Tanioka (2018) to reproduce the tsunami height distribution correctly and
421 make it available for tsunami data assimilation.

422 The warning system that we proposed is applicable not only to seismogenic tsunamis, but
423 also to landslide and volcanic tsunamis. This is extremely helpful in the EMB, due to its potential
424 for a large variety of tsunamigenic sources (Soloviev, 1990). Traditional methods may fail to
425 provide early warnings for non-seismic tsunamis. Our approach is also useful in other regions
426 worldwide where tsunamis are also generated by landslide or volcano eruption, like Indonesia
427 and Japan (Satake, 2007; Maeno et al., 2011; Heidarzadeh et al., 2020). Our designed early
428 warning system aims to solely protect Crete Island, where high possibilities of tsunami
429 occurrences exist. In case the warning system is aimed at protecting other regions such as Cyprus
430 and west Turkey region, a new network of OBPG should be designed.

431

432 **5 Conclusion**

433 We propose a potential early tsunami warning system based on tsunami data
434 assimilation in the Eastern Mediterranean Basin (EMB). Twelve Offshore Bottom Pressure
435 Gauge (OBPGs) are designed around Crete Island, and their locations are confirmed by
436 performing Empirical Orthogonal Function (EOF) analysis. Our proposed warning system is able
437 to forecast tsunami arrival time and amplitude in Crete Island accurately at 10-20 min before the
438 tsunami arrival. The forecasting accuracy of the hypothetical seismogenic tsunami in east Sicily
439 is 88.5%. It also works well for landslide tsunamis, though the high-frequency components of
440 landslide-generated waves are not fully captured by the OBPG network. The forecasting
441 accuracy of our data assimilation approach for the hypothetical landslide tsunami is 85.3%.
442 Moreover, the retrospective study of the real tsunami event of 2 May 2020, generated by an Mw
443 6.6 earthquake off Crete Island, shows that our approach is able to predict the tsunami fairly well
444 though it is a near-field tsunami with travel time of ~20 min. The observed and forecasted first-
445 peak amplitudes are 5.0 cm and 4.5 cm, while the arrival times are 18 min and 19 min,

446 respectively. A warning lead time of ~10 min was obtained for the May 2020 event. We
447 conclude that the deployment of OBPGs is helpful to tsunami early warning for Crete Island for
448 both near-field and far-field tsunamis in the EMB. We recommend this method for other
449 tsunamigenic zones in the EMB region such as the Aegean Sea and west Turkey and for beyond
450 EMB such as Indonesia.

451

452

453 **Acknowledgments**

454 The bathymetry data used in this work comes from the General Bathymetric Chart of the Ocean
455 (GEBCO) (https://www.gebco.net/data_and_products/gebco_digital_atlas/). Sea level data are
456 from the National Observatory of Athens (NOA) (<http://www.noa.gr/index.php?lang=en>) and the
457 Intergovernmental Oceanographic Commission (IOC) ([http://www.ioc-](http://www.ioc-sealevelmonitoring.org/station.php?code=avon)
458 [sealevelmonitoring.org/station.php?code=avon](http://www.ioc-sealevelmonitoring.org/station.php?code=avon)). We used the *JAGURS* tsunami simulation code
459 (Baba et al., 2015; available at <https://github.com/jagurs-admin/jagurs>) and the TDAC data
460 assimilation code (Maeda et al., 2015; available at <https://github.com/takuto-maeda/tdac>). This
461 work is partly supported by the Royal Society, UK, grant number CHL\R1\180173 (MH), JSPS
462 KAKENHI 16H01838 (KS) and 19J20293 (YW). YW thanks Dr. Zhouqiao Zhao of Peking
463 University for his help with job script.

464

465

466 **References**

467 Baba, T., Hirata, K., & Kaneda, Y. (2004). Tsunami magnitudes determined from ocean-bottom
468 pressure gauge data around Japan, *Geophys. Res. Lett.*, 31, L08303,
469 doi:10.1029/2003GL019397.

- 470 Baba, T., Takahashi, N., Kaneda, Y., Ando, K., et al. (2015). Parallel implementation of
471 dispersive tsunami wave modeling with a nesting algorithm for the 2011 Tohoku Tsunami,
472 *Pure Appl. Geophys.*, 172, 3433-3472, doi: 10.1007/s00024-015-1049-2.
- 473 Cohen, K., Siegel, S., McLaughlin, T. (2003). Sensor placement based on proper orthogonal
474 decomposition modeling of a cylinder wake. In 33rd AIAA Fluid Dynamics Conference,
475 Orlando (Vol. 4259, pp. 2003–4259). Orlando, FL: AIAA. doi:10.2514/6.2003-4259.
- 476 Dogan, G. G., Annunziato, A., Papadopoulos, G. A., Guler, H. G., et al. (2019). The 20th July
477 2017 Bodrum-Kos Tsunami Field Survey. *Pure Appl. Geophys.*, 176, 2925-2949.
478 doi:10.1007/s00024-019-02151-1.
- 479 Dominey-Howes, D. T. M., Papadopoulos, G. A., Dawson, A. G. (2000). Geological and
480 historical investigation of the 1650 Mt. Columbo (Thera Island) eruption and tsunami,
481 Aegean Sea, Greece. *Nat. Hazards*, 21, 83-96. doi:10.1023/A:1008178100633.
- 482 Furumura, T., Maeda, T., Oba, A. (2018). Early forecast of long-period ground motions via data
483 assimilation of observed ground motions and wave propagation simulations. *Geophys. Res.
484 Lett.*, 46, 138-147. doi:10.1029/2018GL081163.
- 485 Furumura, T., Saito, T. (2009). Integrated ground motion and tsunami simulation for the 1944
486 Tonankai earthquake using high-performance supercomputers. *J. Disaster Res.*, 4, 118-126.
487 doi:10.20965/jdr.2009.p0118.
- 488 Gusman, A. R., Mulia, I. E., Satake, K., Watada, S., et al. (2016). Estimate of tsunami source
489 using optimized unit sources and including dispersion effects during tsunami propagation:
490 The 2012 Haida Gwaii earthquake. *Geophys. Res. Lett.*, 43, 9819-9828.
491 doi:10.1002/2016GL070140.
- 492 Heidarzadeh, M., Gusman, A. R. (2018). Application of dense offshore tsunami observations
493 from Ocean Bottom Pressure Gauges (OBPGs) for tsunami research and early warnings. In
494 book: *Geological Disaster Monitoring Based on Sensor Networks*, pp.7-22.
495 doi:10.1007/978-981-13-0992-2_2.
- 496 Heidarzadeh, M., Ishibe, T., Sandanbata, O., Muhari, A., et al. (2020). Numerical modeling of
497 the subaerial landslide source of the 22 December 2018 Anak Krakatoa volcanic tsunami,
498 Indonesia. *Ocean Eng.*, 195, 106733. doi:10.1016/j.oceaneng.2019.106733.

- 499 Heidarzadeh, M., Krastel, S., Yalciner, A. C. (2014). The State-of-the-Art Numerical Tools for
500 Modeling Landslide Tsunamis: A Short Review. In: Submarine Mass Movements and Their
501 Consequences, Chapter 43, 483-495, ISBN: 978-3-319-00971-1, Springer International
502 publishing. doi:10.1007/978-3-319-00972-8_43.
- 503 Heidarzadeh, M., Necmioglu, O., Ishibe, T., Yalciner, A. C. (2017). Bodrum-Kos (Turkey-
504 Greece) Mw 6.6 earthquake and tsunami of 20 July 2017: a test for the Mediterranean
505 tsunami warning system. *Geoscience Lett.*, 4:31. doi:10.1186/s40562-017-0097-0.
- 506 Heidarzadeh, M., Satake, K. (2013). The 21 May 2003 tsunami in the Western Mediterranean
507 Sea: Statistical and wavelet analyses. *Pure Appl. Geophys.*, 170(9), 1449-1462.
508 doi:10.1007/s00024-012-0509-1.
- 509 Heidarzadeh, M., Wang, Y., Satake, K., Mulia, I. E. (2019). Potential deployment of offshore
510 bottom pressure gauges and adoption of data assimilation for tsunami warning system in the
511 western Mediterranean Sea. *Geoscience Lett.*, 6:19. doi:10.1186/s40562-019-0149-8.
- 512 Kaneda, Y. (2010). The advanced ocean floor real time monitoring system for mega thrust
513 earthquakes and tsunamis-application of DONET and DONET2 data to seismological
514 research and disaster mitigation-. *OCEAN 2010*. doi:10.1109/OCEANS.2010.5664309.
- 515 Kawamata, K., Takaoka, K., Ban, K., et al. (2005). Model of tsunami generation by collapse of
516 volcanic eruption: The 1741 Oshima-Oshima tsunami, in *Tsunamis: Case Studies and*
517 *Recent Developments*, edited by K. Satake, 79-96, Springer, New York.
- 518 Lorentz, E. N. (1956). Empirical Orthogonal Functions and statistical weather prediction. In
519 Statistical Forecasting Report: Scientific Report No. 1 (pp. 49). Cambridge: Massachusetts
520 Institute of Technology, Department of Meteorology.
- 521 Maeda, T., Obara, K., Shinohara, M., Kanazawa, T., et al. (2015). Successive estimation of a
522 tsunami wavefield without earthquake source data: A data assimilation approach toward
523 real-time tsunami forecasting. *Geophys. Res. Lett.*, 42, 7923-7932.
524 doi:10.1002/2015GL065588.
- 525 Maeno, F., Imamura, F. (2011). Tsunami generation by a rapid entrance of pyroclastic flow into
526 the sea during the 1883 Krakatau eruption, Indonesia. *J. Geophys. Res.*, 116, B09205.
527 doi:10.1029/2011JB008253.

- 528 Mulia, I. E., Gusman, A. R., Satake, K. (2017). Optimal design for placements of tsunami
529 observing systems to accurately characterize the inducing earthquake. *Geophys. Res. Lett.*
530 44, 12106-12115. doi:10.1002/2017GL075791.
- 531 Mulia, I. E., Gusman, A. R., Williamson, A. L., Satake, K. (2019). An optimized array
532 configuration of tsunami observation network off Southern Java, Indonesia. *J. Geophys.*
533 *Res. Solid Earth*, 124(9), 9622-9637. doi:10.1029/2019JB017600.
- 534 Navarrete, P., Cienfuegos, R., Satake, K., Wang, Y., et al. (2020). Sea surface network
535 optimization for tsunami forecasting in the near field: Application to the 2015 Illapel
536 earthquake. *Geophys. J. Int.*, 221, 1640-1650. doi:10.1093/gji/ggaa098.
- 537 Okada, Y. (1985). Surface deformation due to shear and tensile faults in a half-space. *B. Seismol.*
538 *Soc. Am.*, 75(4), 1135-1154.
- 539 Okal, E. A., Synolakis, C. E., Uslu, B., Kalligeris, N., Voukouvalas, E. (2009). The 1956
540 earthquake and tsunami in Amorgos, Greece. *Geophys. J. Int.*, 178, 1533-1554.
541 doi:10.1111/j.1365-246X.2009.04237.x.
- 542 Papadopoulos, G. A., Daskalaki, E., Fokaefs, A. (2007a). Tsunamis Generated By Coastal And
543 Submarine Landslides In The Mediterranean Sea. In: *Lykousis V., Sakellariou D., Locat J.*
544 *(eds) Submarine Mass Movements and Their Consequences. Advances in Natural and*
545 *Technological Hazards Research*, vol 27. Springer, Dordrecht. doi:10.1007/978-1-4020-
546 6512-5_43.
- 547 Papadopoulos, G. A., Daskalaki, E., Fokaefs, A., Giraleas, N. (2007b). Tsunami hazards in the
548 Eastern Mediterranean: strong earthquakes and tsunamis in the East Hellenic Arc and
549 Trench system. *Nat. Hazard Earth Sys.*, 7(1), 57-64. doi:10.5194/nhess-7-57-2007.
- 550 Ren, Z., Wang, Y., Wang, P., Hou, J., et al. (2020). Numerical Study of the Triggering
551 Mechanism of the 2018 Anak Krakatau Tsunami: Eruption or Collapsed landslide? *Nat.*
552 *Hazards*, 102, 1-13. doi:10.1007/s11069-020-03907-y.
- 553 Samaras, A. G., Karambas, T. V., Archetti, R. (2015). Simulation of tsunami generation,
554 propagation and coastal inundation in the Eastern Mediterranean. *Ocean Sci.*, 11, 643-655.
555 doi:10.5194/os-11-643-2015.

- 556 Satake, K. (1995). Linear and nonlinear computations of the 1992 Nicaragua earthquake
557 tsunami. *Pure Appl. Geophys.* 144(3-4), 455-470. doi:10.1007/BF00874378.
- 558 Satake, K. (2007). Volcanic origin of the 1741 Oshima-Oshima tsunami in the Japan Sea. *Earth*
559 *Planets Space*, 59(5), 381-390. doi:10.1186/BF03352698.
- 560 Satake, K. (2012). Tsunamis generated by submarine landslides. In *Submarine mass movements*
561 *and their consequences* (pp. 475-484). Springer, Dordrecht.
- 562 Satake, K. (2014). Advances in earthquake and tsunami sciences and disaster risk reduction since
563 the 2004 Indian ocean tsunami. *Geoscience Lett.*, 1:15. doi:10.1186/s40562-014-0015-7.
- 564 Satake, K. (2015). Tsunamis. In: Schubert G (ed) *Treatise on Geophysics*, 2nd edn, Vol 4.
565 Elsevier, Oxford, p477-504.
- 566 Shaw, B., Ambraseys, N. N., England, P. C., Floyd, M. A., et al. (2008). Eastern Mediterranean
567 tectonics and tsunami hazard inferred from the AD 365 earthquake. *Nat. Geosci.*, 1, 268-
568 276. doi:10.1038/ngeo151.
- 569 Soloviev, S. L. (1990). Tsunamigenic zones in the Mediterranean Sea. *Nat. Hazards*, 3, 183–202.
570 doi:10.1007/BF00140432.
- 571 Tanioka, Y. (2018). Tsunami Simulation Method Assimilating Ocean Bottom Pressure Data
572 Near a Tsunami Source Region. *Pure Appl. Geophys.*, 175, 721-729. doi:10.1007/s00024-
573 017-1697-5.
- 574 The United States Geological Survey (USGS). Information on M 6.6 - 89km S of Ierapetra,
575 Greece. <https://earthquake.usgs.gov/earthquakes/eventpage/us700098qd/executive>.
576 Accessed 2 May 2020.
- 577 Wang, Y., Satake, K., Maeda, T., Gusman, A. R. (2017). Green's Function-based Tsunami Data
578 Assimilation (GFTDA): A fast data assimilation approach toward tsunami early warning.
579 *Geophys. Res. Lett.*, 44, 10282-10289. doi:10.1002/2017GL075307.
- 580 Wang, Y., Satake, K., Maeda, T., Gusman, A. R. (2018). Data assimilation with dispersive
581 tsunami model: a test for the Nankai Trough. *Earth Planets Space*, 70, 131.
582 doi:10.1186/s40623-018-0905-6.

- 583 Wang, Y., Satake, K., Sandanbata, O., Maeda, T., et al. (2019). Tsunami data assimilation of
584 cabled ocean bottom pressure records for the 2015 Torishima volcanic tsunami earthquake.
585 *J. Geophys. Res. Solid Earth*, 124, 10413-10422. doi:10.1029/2019JB018056.
- 586 Weatherall, P., Marks, K. M., Jakobsson, M., Schmitt, T., et al. (2015). A new digital
587 bathymetric model of the world's oceans. *Earth Space Sci.*, 2, 331–345.
588 doi:10.1002/2015EA000107.
- 589 Yalciner, A. C., Zaytsev, A., Aytore, B., Insel, I., et al. (2014). A Possible Submarine Landslide
590 and Associated Tsunami at the Northwest Nile Delta, Mediterranean
591 Sea. *Oceanography*, 27(2), 68-75. doi:10.5670/oceanog.2014.41.
- 592 Yalciner, A. C., Annunziato, A., Papadopoulos, G., Dogan, G. G., et al. (2017). The 20th July
593 2017 (22:31 UTC) Bodrum/Kos earthquake and tsunami: post tsunami field survey report.
594 [http://users.metu.edu.tr/yalciner/july-21-2017-tsunami-report/Report-FieldSurvey-of-July-](http://users.metu.edu.tr/yalciner/july-21-2017-tsunami-report/Report-FieldSurvey-of-July-20-2017-Bodrum-Kos-Tsunami.pdf)
595 [20-2017-Bodrum-Kos-Tsunami.pdf](http://users.metu.edu.tr/yalciner/july-21-2017-tsunami-report/Report-FieldSurvey-of-July-20-2017-Bodrum-Kos-Tsunami.pdf). Accessed 30 March 2018.
- 596
- 597
- 598